Composites Science and Technology 58 (1998) 1335–1341

Printed in Great Britain
0266-3538/98 $—see front matter

PII: S0266-3538(98)00006-2

PREDICTION AND MEASUREMENT OF THE POST-CRITICAL BEHAVIOR OF FIBER-REINFORCED COMPOSITE COLUMNS

E. J. Barbero[a]* & J. Trovillion[b]

[a]*Mechanical and Aerospace Engineering, West Virginia University, Morgantown, WV 26506-6106, USA*
[b]*Civil Engineering Research Lab, U.S. Army Corps of Engineers*

(Received 11 February 1997; accepted 9 January 1998)

Abstract
Experimental measurements on axially loaded columns made of fiber-reinforced composite materials are presented. Experimental load/deflection plots at twelve flange points and three web points allow for an accurate description of the deformations, including the post-critical behavior. Data processing by two methods is described and a comparison is made between the two methods. In one method, the incipient buckling data are used, while in the second method, the post buckling data are used. The effect of damage accumulation is illustrated. The behavior, including the curvature of the post-critical path, is predicted by using stability theory. Comparisons between predicted and measured values of critical load and post-critical path curvature are presented. © 1998 Elsevier Science Ltd. All rights reserved

1 INTRODUCTION

Pultruded structural shapes are used for civil-engineering construction when corrosion resistance is important.[1] Pultruded structural shapes resemble cold-rolled steel structural shapes and they are used as a direct replacement for steel. The material used is a fiber reinforced composite produced by pultrusion from high-strength E-glass fibers embedded in a vinyl ester or polyester polymer resin. The composite material is quite strong (up to 482 MPa in compression[2], less stiff than steel (up to 50 GPa), and more expensive (2 to 8 US $ kg^{-1}). For these reasons, and because of limitations on the maximum thickness that can be produced by pultrusion, all pultruded structural shapes are thin-walled structures. Consequently, local buckling controls the failure of these products when used as columns. Bracing is usually employed as an inexpensive way to control global (Euler) buckling. Since the material remains linearly elastic in the region of interest[3], prediction of the critical load and the post-critical path can be done in the context of elastic stability.[4]

*To whom correspondence should be addressed.

2 COLUMN SAMPLES

Three types of samples were used in this investigation. All have the same cross-section, in the shape of a wide-flange I section of width and depth $b=d=304{\cdot}8$ mm, with both flanges and the web having thickness $t=12{\cdot}7$ mm. The area of the cross-section is $S=112{\cdot}9\,\text{cm}^2$, and the area moment of inertia is $I=5998{\cdot}5\,\text{cm}^4$.

The difference among the samples is the fiber reinforcement used. The first section, labeled CP, contains roving (unidirectional fibers) and continuous strand mat (CSM), with predicted stiffness given in Table 1. The second section, labeled F1, contains additional roving and CSM to achieve higher extensional and bending stiffness. The third section, labeled F2, contains additional stitched bidirectional fibers to achieve higher local buckling load. Note that the global buckling (Euler) load can be accurately predicted from the bending stiffness[5] using the standard column buckling load equation

$$P^{CR}=\frac{\pi^2(EI)}{L^2} \tag{1}$$

Note that because of the various materials and fiber orientations used in the cross-section, the term (EI) cannot be separated into a stiffness E and a moment of inertia I, as it is done for steel sections. Also, the extensional and bending stiffness of these sections can be accurately predicted using the analysis presented.[6] The length of the columns (see Table 1) used for testing were chosen to correspond to three local buckling half-waves (Table 1), predicted using the model described in Section 5.

3 EXPERIMENTAL PROCEDURE

The samples were loaded with an MTS hydraulic machine with load capacity 4·454 MN (Fig. 1) at a loading rate of 1·27 mm min^{-1}. The samples were

Table 1. Sample length and structural properties

Material type	Sample length (m)	Axial stiffness ES (MN)	Bending stiffness EI (MN m^2)
CP	1·816	289·887	1·511
F1	1·499	363·920	1·917
F2	1·511	333·916	1·740

clamped at the ends by potting them with a room-temperature polyester resin into steel groved end-fixtures (Fig. 2). Since the polyester resin is flexible, the effect of the end-fixtures is to introduce an approximately simply-supported condition for each panel (flange and web) while restricting any distortion of the cross-section. The end-fixtures rest on fixed flat plates on the Universal Testing System (UTS). Therefore, from a global point of view, the column is under fixed-end conditions.

Flange deflections were continuously recorded, along with the load, using a data acquisition system on a personal computer. The position of the linear variable differential transducers (LVDT) is shown in Fig. 1. A set of typical load–deflection curves for one of the columns is shown in Fig. 3.

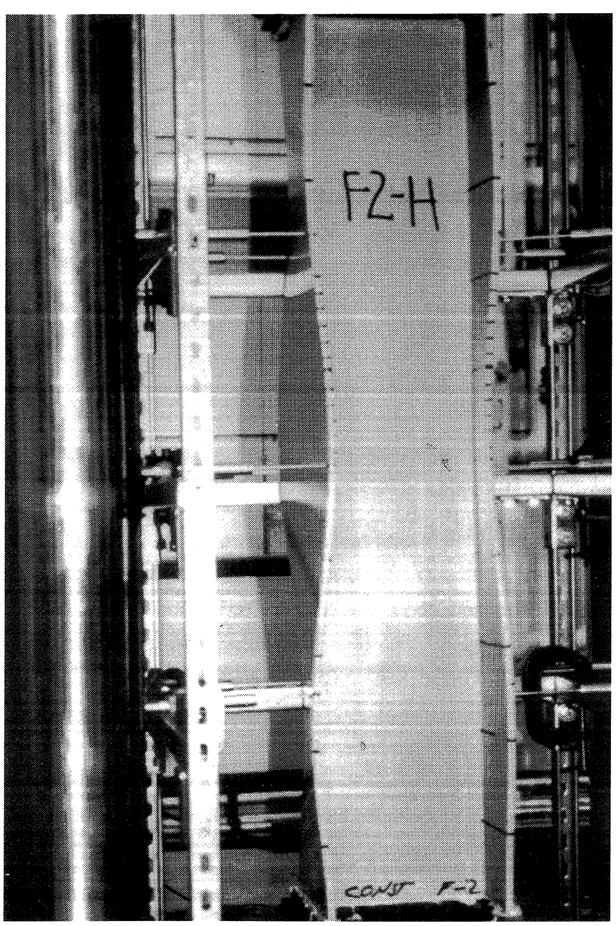

Fig. 1. Testing setup for sample H of material F2.

4 DATA REDUCTION

The objective of data reduction schemes is to infer the critical load, P^{CR}, and the curvature of the post-critical path, $P^{(2)}$, of the column. These values are necessary for the design of structures where such columns may be used. Since the samples contain imperfections, non-zero deflections are recorded for all values of the load, making it difficult to identify the critical load directly from the load–deflection plot (Fig. 3).

In the case of local buckling, the location of the maximum deflection of the buckling mode is not known a priori, unlike the case of global buckling where the maximum deflection occurs at the mid-span. Therefore, the magnitude of displacement recorded by the transducers depends on their location along the length of the column. Also, the load displacement data may have more or less deflection for a given load depending of the magnitude of the imperfections. It is therefore necessary to process the data to obtain a critical load and post-critical curvature, independently of the magnitude of the imperfection and the position of the transducers.

4.1 Modified Southwell method

Southwell's method, conceived for global buckling[7], was extended to the case of local buckling[8] taking into account that the displacement transducers may not be placed at the point of maximum deflections of the buckling mode. Basically, the load/deflection data are assumed to have an hyperbolic shape (Fig. 4). Then, by plotting the transformed data (deflection/load vs deflection, Fig. 5), a straight line is obtained and a linear regression can be done to find the slope and the abscissa at zero load. The inverse of the slope in Fig. 5 is the critical load, or asymptote of the load/deflection curve in Fig. 4. The abscissa at zero load gives an indication of the imperfections in the sample.[8] However, previous work did not take into account the stiffening of the system along the post-critical path. This stiffening is investigated here.

Southwell's method assumes that the load–deflection curve of an imperfect column has an hyperbolic shape (Fig. 4). The method seeks to find the asymptote of the hyperbola assuming that the post-critical path is flat (constant load). This leads to correct results for the case of global buckling because the stiffening of the post-critical path is very small. But for local buckling, the stiffening of the post-critical path may be considerable (Fig. 3). In this case, the post-critical data may corrupt the results of the method leading to an artificially high critical load. The magnitude of the induced error depends of the curvature of the post-critical path. The maximum error encountered in this investigation was 22% with respect to the value obtained using the quadratic approximation described in the next section.

The values of the critical load P^{CR} are reported in Table 2 with the 95% confidence interval given in parentheses. Southwell's method provides the critical load

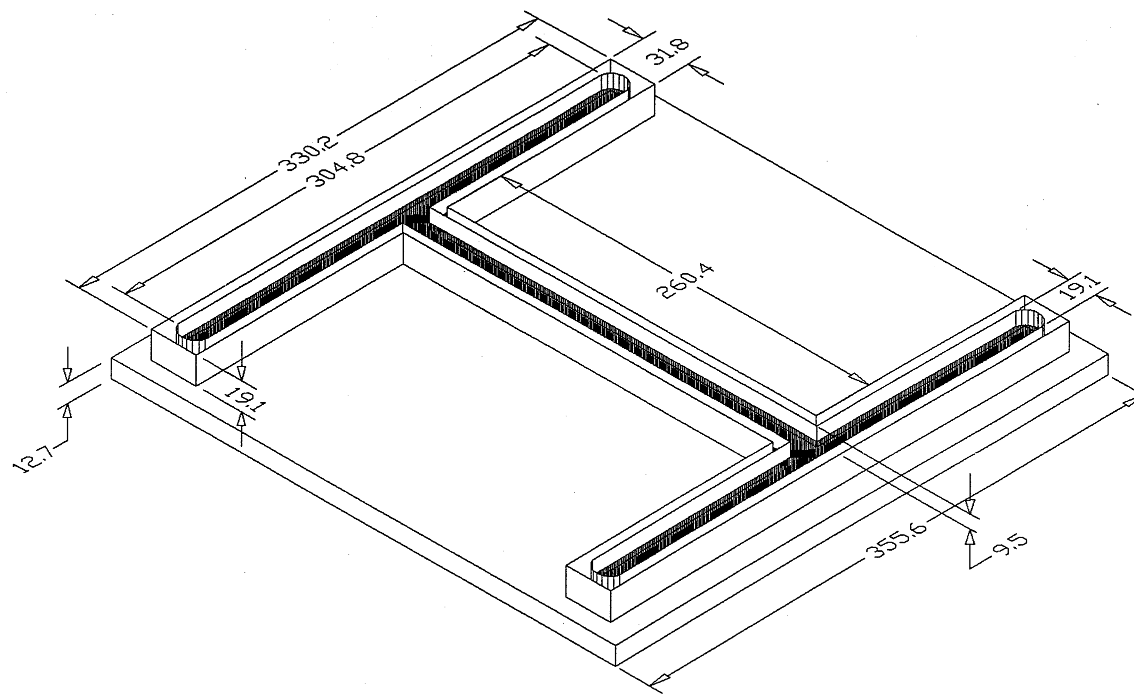

Fig. 2. Schematic of the end-grip used to support the sample.

only, with no provision for the computation of the curvature of the post-critical path.

4.2 Quadratic approximation of the post-critical path

Based on the experimental observations (Fig. 6), it is clear that the post-critical path can be accurately approximated by a quadratic expansion of the load

$$P = P^{CR} + \frac{1}{2}P^{(2)}s^2 \tag{2}$$

where P^{CR} is the critical load, $P^{(2)}$ is the curvature of the post-critical path, P is the axial load, and s is the perturbation parameter. This expansion is similar to the perturbation expansion used for post buckling analysis.[4] While the critical load P^{CR} is independent of which perturbation parameter is chosen, the curvature of the post-critical path depends of which perturbation parameter is chosen. In this study, two possibilities exist for the selection of the perturbation parameter.

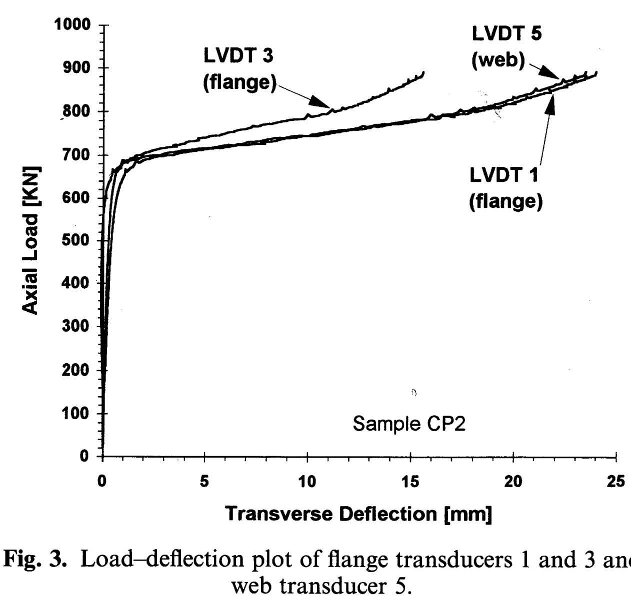

Fig. 3. Load–deflection plot of flange transducers 1 and 3 and web transducer 5.

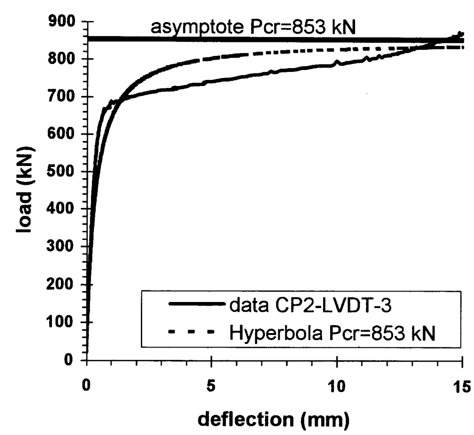

Fig. 4. Comparison of actual data with assumed hyperbolic behavior.

Consider an I-section with the axis of the column oriented along the z-coordinate axis and web on the y–z plane. In addition, the flange and web have both width b and the columns is loaded at the origin. If the axial displacement under the load is chosen as the perturbation parameter ($s=\omega(0,0,0)$), the curvature in the load–stroke space is $P^{(2)}_{stroke}$. If the maximum deflection at the tip of a flange is used as a perturbation parameter ($s=v(b/2,b/2,z^*)$), the curvature in the load-flange-deflection space is $P^{(2)}_{flange}$. In the later case z^* indicates the position of maximum flange deflection. While the

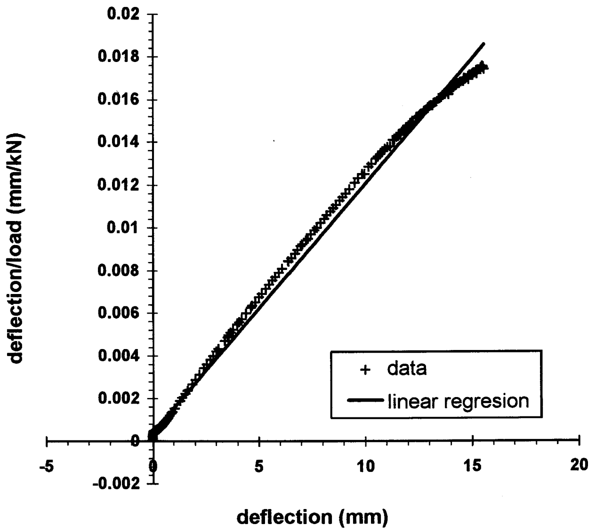

Fig. 5. Experimental data in Southwell's format.

Table 2. Critical loads (95% confidence interval in parentheses)

	CP	F1	F2
Pcr Southwell [kN]	724·51 (279·79)	1169·19 (16·57)	1192·21 (35·66)
Pcr Quadratic [kN]	698·31 (6·71)	954·72 (25·03)	1139·36 (17·73)
Pcr FEM [kN]	660·46	866·26	1207·52

numerical values of curvature $P^{(2)}_{stroke}$ and $P^{(2)}_{flange}$ are different, the predicted load computed using eqn (2) and the appropriate perturbation parameter should be identical. Note in Tables 3 and 4 that $P^{(2)}_{flange} \ll P^{(2)}_{stroke}$ because the flanges loose most of their the stiffness when they buckle, while the axial stiffness of the column (in the stroke direction) remains high even after the flanges have buckled.

The most accurate measurements of deflection are those corresponding to flange deflection data ($v(b/2,b/2,z)$). However, there is no assurance that the transducers measure the deflection at the maximum of the mode shape because the transducers are installed at arbitrary locations that may not coincide with the points of maximum deflection. On the numerical model, the perturbation parameter was chosen as the maximum deflection of the mode shape. The measured and predicted values are shown in Table 3. Some inaccuracy in the measurement of the curvature $P^{(2)}_{flange}$ for the CP samples is likely caused by the fact that only two samples were available for testing. Since the finite element

Table 3. Post-critical curvature of load vs flange-deflection plot (95% confidence interval in parentheses)

	CP	F1	F2
$P^{(2)}_{flange}$ Experimental [kN mm^{-2}]	0·48 (0·43)	1·48 (0·45)	1·52 (0·66)
$P^{(2)}_{flange}$ FEM [KN mm^{-2}]	1·09	1·30	1·36

Table 4. Post-critical curvature of load vs stroke plot (95% confidence interval in parentheses)

	CP	F1	F2
$P^{(2)}_{stroke}$ Experimental [kN mm^{-2}]	42·84 (1·35)	73·69 (3·92)	72·28 (12·68)
$P^{(2)}_{stroke}$ FEM [kN mm^{-2}]	50·86	28·57	80·05

solution provides the postbuckling mode shape, the measured deflections at the positions of the transducers could be used to extrapolate the maximum deflection on the basis of the computed mode shape. This could give a more accurate prediction for the curvature of the post-critical path based on transducer data.

The axial displacement ($\omega(0,0,0)$) was measured during the test as the stroke of the testing machine. Therefore, the curvature of the post-critical path can be evaluated from the load–stroke experimental data. The measured and predicted values are indicated in Table 4.

For each of the fifteen load–deflection curves available for each specimen, the post-critical path was fitted with eqn (2). The data corresponding to flange or web deflections larger than $t/10$ was used, where t is the thickness of the panel ($t = 12{\cdot}7$ mm in this case). A typical fit is shown in Fig. 6. The values of the critical load are reported in Table 2. The values of the critical load computed by Southwell's method are included for comparison.

4.3 Effect of damage accumulation

The data must be collected during the first loading of the column, as the test introduces damage in the material when the deformations are large. Finite element analysis indicates that the material remains linear up to buckling but becomes non-linear during post buckling because of the large deformations that occur at this stage. To investigate the effect of damage, the columns were re-loaded for a second time after the initial test. When the initial test involved large post buckling deflections, the re-loading load–deflection curve shows evidence of deterioration of the material, as it can be seen in Fig. 7.

The effect of damage is equivalent to a magnification of the initial imperfections in the column. The mode shape developed during re-loading is identical to the mode shape of the first test but the deflections are more noticeable at smaller values of the load. However, Southwell data reduction leads to similar values for the critical load.

The load–displacement data from LVDT number 1 of sample CP2 during the first (undamaged) and second (damaged) loading is shown in Fig. 7. The same data, represented in the format used in the Southwell method are shown in Fig. 8. The predicted critical loads are 852 and 922 kN for the undamaged and damaged cases.

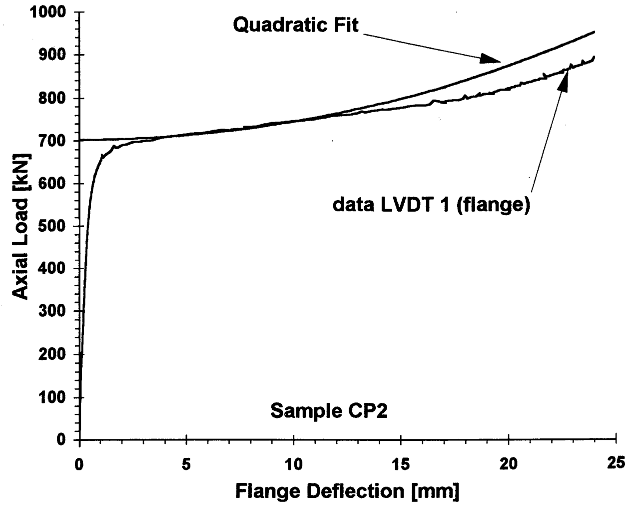

Fig. 6. Quadratic fit of the post-critical experimental data.

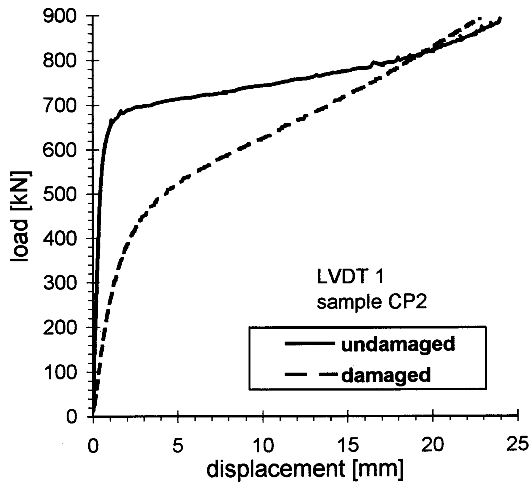

Fig. 7. Effect of damage accumulation on the load–deflection behavior.

The similarity of the predicted critical loads is because both load–deflection plots seem to approach similar asymptotes of load. In fact, the slope of the two curves in Fig. 8 are very similar, especially if the data for large displacements are disregarded. Therefore, the damage accumulated during the first loading of the column acts as a magnification of the imperfections but it does not degrades the load-carrying capacity of the column during post-buckling.

5 FINITE ELEMENT MODEL

Buckling and post buckling analysis was performed using the finite element code.[9,10] While the buckling load and buckling mode shape can be obtained by a number of commercial finite element packages, none of the commonly available packages can predict the curvature of the post-critical path without performing an expensive fully non-linear analysis. For this reason, a

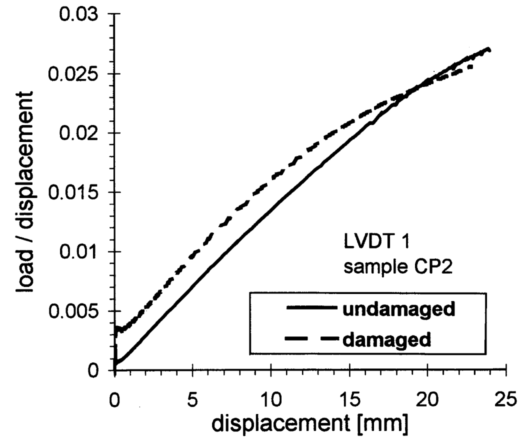

Fig. 8. Damaged and undamaged data in Southwell's format.

computer code based on perturbation techniques was developed.[9,10]

Not only can the curvature of the post-critical path be obtained but also the possibility of having two or more interacting modes can be evaluated.[11,12] When two buckling modes have bifurcation loads that are close or even coincident, the two modes may interact and form a new mode. While the two isolated modes may have stable post-critical path (as shown in Fig. 3), the new mode may have an unstable post-critical path. In this case, the actual load that can be sustained by the imperfect structure will in general be significantly lower than the predicted, isolated mode, bifurcation load. In this case, the structure is called an imperfection sensitive system. This type of behavior has been shown in[13] for pultruded structural shapes similar to the ones used in this study. Therefore, when buckling mode interaction is a possibility, the critical, or bifurcation load provided by standard finite element packages may be of little significance to the designer, who should be aware of a possible reduction of the actual failure load with respect to the bifurcation value. Interacting modes were avoided in this study by selecting a sample length much shorter than the critical interaction length.

One half of the length of the column was modeled because of symmetry. The finite element model consist of 120 elements distributed in 20 sets along the length, each set having 6 elements to describe the cross-section. All elements are Lagrangean quadratic elements with 9 nodes. One element was used for each flange and two to represent the web. From a convergence study that was carried out, this was the minimum mesh refinement necessary for 2% accuracy on the critical load.

The material properties of the composite material were computed for flange and web using the lay-up information from the manufacturing process. A representative description of the fiber architecture used in sample F1 is shown in Fig. 9. First, each panel (flange or web) of the section is idealized as a stack of layers. Each layer corresponds to a different fiber architecture used during pultrusion (roving, continuous strand mat, bidirectional stitched mat, etc.). For each layer the fiber

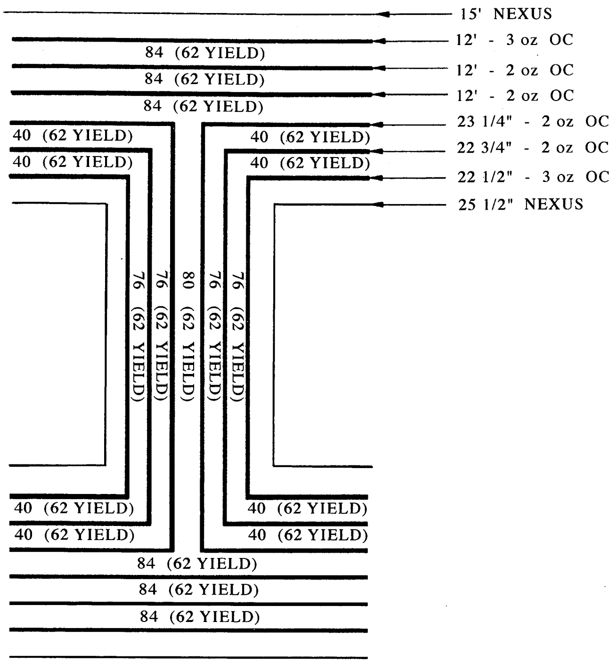

Fig. 9. Fiber architecture of samples F1.

volume fraction is computed based on the weight of the fibers in that layer. For roving layers

$$V_f = \frac{NR}{b} \frac{TEX}{10,000 \rho t_c} \tag{3}$$

where TEX is the weight of the roving in gr Km^{-1}, ρ is the density of the fibers (2·5 gr cc^{-1}), b is the width of the panel in cm, and t_c is the thickness of the layer in mm. The TEX can be computed from the yield Y yd lb^{-1}, which is used in the U.S., as

$$TEX[gr/km^{-1}] = \frac{496,238}{Y[yd/ib^{-1}]} \tag{4}$$

Since layers are not clearly defined in the pultruded product, the thickness of the layers are selected so that the fiber volume fraction is approximately uniform through the cross-section and equal to the overall fiber volume fraction of the panel. Also, the thickness of various layers are selected so that the total thickness of the lay-up be equal to the thickness of the pultruded part (12·7 mm in this study).

For continuous strand mat (CSM) and bidirectional stitched mat ($\pm\theta$) layers, the fiber volume fraction is computed as

$$V_f = \frac{\omega}{1000 \rho t_c} \tag{5}$$

where w is the weight of the mat in gr m^{-2}, ρ is the density of the fibers (2·5 gr cc^{-1}) and t_c is the thickness of the layer in mm.

Knowing the fiber volume fraction and the basic elastic properties of the E-glass fibers (E=72·345 MPa, ν=0·22) and the matrix (Vinyl Ester Ashland D-1419, E=4·051 MPa, ν=0·24), the periodic microstructure model[14] is used to predict the stiffness properties of each layer. Then, Classical Lamination Theory (CLT)[15] is used to compute the stiffness of the panel (flange or web), that is the A, B, and D matrices of the flange and the web. These matrices are then provided as input to the finite element code.

The finite element code was used to predict the critical load and the curvature of the post-critical path. The curvature of the post-critical $P^{(2)}$ can be used to predict the load P during the post-critical path according to eqn (2). The predicted values are compared to the experimental values in Tables 2–4. The numerical predictions of critical load are within 9·3% of the experimental values. This is considered quite accurate taking into account that the material properties were computed from matrix and fiber data using micromechanics. Using First Order Shear Deformation Theory (FSDT) instead of CLT did not affect the critical loads significantly. Any discrepancies between numerical and experimental results are most likely the result approximations in the prediction of the stiffness coefficients.

When the flange displacement was used to compute the curvature of the post-critical path for samples F1 and F2, the predicted values were within 12·1% of the measured values. The error and the 95% confidence interval was larger for the CP samples, likely because only two samples were available for testing·

Finally, the stroke was used to compute the curvature of the post-critical path. The number of readings of stroke data was too small in the case of samples F1 to allow for accurate measurement of the curvature $P^{(2)}_{stroke}$. The data acquisition rate was corrected for samples F2, obtaining as low as 10·8% difference between the predicted and measured values.

6 CONCLUSIONS

The fit of the post-critical deformations provides an accurate measurement of the critical load and the curvature of the post-critical path for fiber reinforced composite columns. The data must be collected during the first loading of the column, as the test introduces damage in the material when the deformations are large. The modeling techniques used, from micromechanics to finite element modeling, proved accurate for predicting the critical load and the curvature of the post-critical path. While the modified Southwell's method is also adequate to obtain the critical load, care must be taken of not using data well into the post-critical path because of the inaccuracies introduced by a stiffening post-critical path.

ACKNOWLEDGEMENTS

The collaboration of Mohammed Al-Megdad and Creative Pultrusions, Inc. for production of the samples is appreciated. The samples were produced and testing was done as part of CPAR–CRDA funded by the U.S. Army Corps of Engineers, with the participation of the Society of Plastic Industry/Composite Institute. The financial support is appreciated. We also acknowledge the collaboration of Edgar Dede during fabrication of the test grips. The first author gratefully acknowledges partial support through NATO grant CGR 960703

REFERENCES

1. Barbero, E. J., Applications: Construction. In *Handbook of Composites*, 2nd edn. Chapman & Hall, 1998.
2. Barbero, E. J. and Tomblin, J. A., Damage mechanics model for compression strength of Composites. *Int. J. Solid Structures*, 1996, **33**(29), 4379–4393.
3. Makkapati, S., Compressive strength of pultruded structural shapes, M.Sc. thesis, West Virginia University, Morgantown, WV, October 1994.
4. Thompson, J. M. and Hunt, G. W., *A General Theory of Elastic Stability*. Wiley, New York, 1973.
5. Barbero, E. J. and Tomblin, J. S., Euler buckling of thin-walled composite columns. *Thin-Walled Structures*, 1993, **17**, 237–258.
6. Barbero, E. J., Lopez-Anido, R. and Davalos, J. F., On the mechanics of thin-walled laminated composite beams. *J. Compos. Mater*., 1993, **27**(8), 806–829.
7. Southwell, R. V., *Theory of Elasticity*. Oxford University Press, London, 1941.
8. Tomblin, J. S. and Barbero, E. J., Local buckling experiments on FRP columns. *Thin-Walled Structures*, 1994, **18**, 97–116.
9. Godoy, L. A., Barbero, E. J. and Raftoyiannis, I., Finite elements for post-buckling analysis—part I: W-formulation. *Computer and Structures*, 1995, **56**(6), 1009–1017.
10. Barbero, E. J., Raftoyiannis, I. and Godoy, L. A., Finite elements for post-buckling analysis—part II: applications to composite plate assemblies. *Computer and Structures*, 1995, **56**(6), 1019–1028.
11. Barbero, E. J., Godoy, L. A. and Raftoyiannis, I., Finite elements for three-mode interaction in buckling analysis. *Int. J. Numer. Meth. Eng*., 1996, **39**, 469–488.
12. Raftoyiannis, I., Godoy, L. A. and Barbero, E. J., Buckling mode interaction in composite plate assemblies, *Appl. Mech. Rev., 48(11, Part 2), November (1995)*.
13. Godoy, L. A., Barbero, E. J. and Raftoyiannis, I., Interactive buckling analysis of fiber-reinforced thin-walled columns, *J. Compos. Mater*., 1995, **29**(5), 591–613.
14. Luciano, R. and Barbero, E. J., Formulas for the stiffness of composites with periodic microstructure. *Int. J. of Solids Structures*, 1995, **31**(21), 2933–2944.
15. Barbero, E. J., *Introduction to Composite Materials Design*. Taylor and Francis, Bristol, PA, in press.